RSC Advances

PAPER

View Article Online
View Journal | View Issue

Cite this: *RSC Adv.*, 2017, **7**, 42476

A facile microwave-assisted approach to the synthesis of flower-like $ZnCo_2O_4$ anode materials for Li-ion batteries

Guang-Hao Shih and Wei-Ren Liu *

A simple and rapid microwave-assisted hydrothermal (MH) method is used to synthesize spinel-based $ZnCo_2O_4$ anode material for Li-ion batteries. Microwaves provide a uniform and rapid formation of the oxide at a low temperature of 190 °C for a short reaction time of 15 minutes. The crystallinity, pore size distribution, surface morphology and characteristics, crystal structure, surface morphologies and electrochemical properties of $ZnCo_2O_4$ (ZCO) are carried out by using X-diffraction (XRD), Brunauer–Emmett–Teller (BET) analysis, scanning electron microscopy (SEM), transmission electron microscopy (TEM), cyclic voltammetry, impedance and cyclic performance, respectively. The initial discharge capacity of microwave-ZCO (M-400) is 1510 mA h g^{-1}, at a current rate of 100 mA g^{-1}. After 30 cycles, the M-400 sample delivers a reversible capacity as high as 1334 mA h g^{-1} at 100 mA g^{-1}. For 10C tests, M-400 demonstrates a capacity of more than 605 mA h g^{-1}, which is superior to that of conventional ZCO samples synthesized by hydrothermal reaction (C-400). In subsequent cycles, the capacity of M-400 recovers to 1664 mA h g^{-1} with the current density back to 0.1C and the diffusivity was higher than C-400 by ~18 times. The comparable high capacity of the MH method indicates that it could be a viable route to easily synthesize spinel oxides.

Received 12th July 2017
Accepted 27th August 2017

DOI: 10.1039/c7ra07660f

rsc.li/rsc-advances

1. Introduction

Lithium-ion batteries (LIBs) are regarded as some of the leading energy storage devices for daily usage[1,2] due to their merits of high energy density, no memory effect, tiny volume and being eco-friendly. Thus, nowadays, LIBs can be used for most primary batteries in the world such as mobile devices, laptops, electric vehicles (EVs), hybrid electric vehicles (HEVs) and so on.[1–6] Typically, LIBs are made from a cathode, anode, separator and electrolyte. In aspects of anode materials, graphite is the primary one used in the current market. Its theoretical capacity of 372 mA h g^{-1} cannot reach the current demands for high energy density.[1,7–9] Accordingly, it is necessary to explore other anode materials which can replace graphite with high energy density, long cycle life and environmentally friendly material in high-performance LIBs. Interestingly, transition-metal oxides, for instance Fe_2O_3,[11–15] NiO[16] and Co_3O_4,[10,17–19] are suitable as promising anode materials as their high capacity is higher than those of conventional graphite based electrodes.[10] It is worth mentioning that Co_3O_4 exhibits great electrochemical performance, theoretical capacity as high as ~900 mA h g^{-1} and excellent cycle life.[20] Co_3O_4 has been extensively studied as an alternative material to graphite for rechargeable lithium batteries.[21] Iron-based spinel oxides, like Co_3O_4, were more stable during discharge/charge process.[10,14,15] However, cobalt is toxic and expensive because of comprising very few metal of the Earth's crust.[22] It is desirable to be made to replace Co in Co_3O_4 by other cheaper and alternative elements which are friendly to environment like MCo_2O_4 (M = Zn, Cu, Ni, Mg, Fe and Mn)[11,18,20,22–26] generally having higher reversible capacity[27] by concluded that metals with inverse spinel structure can be incorporated with more Li ions, compared to mixed and normal spinel.[15,28] Various chemical and physical methods have been adopted for the preparation of these metal oxides.[29] $ZnCo_2O_4$ is an isomorphic material to Co_3O_4 for evaluation as anode for LIBs. There was great interest in oxide anodes based on conversion and alloying–dealloying/conversion reactions[13] and $ZnCo_2O_4$ has an inverse spinel structure with Zn^{2+} and half of the Co^{3+} cation occupying the octahedral site and the remaining Co^{3+} on the tetrahedral site, $Co^{3+}[Zn^{2+}, Co^{3+}]O_4$.[15] It, reversible capacity of ~960 mA h g^{-1}, is a spinel crystallize structure with Zn^{2+}.[20,30–35] According to studies, the excellent electrochemical performance depends on the nanostructure. It makes $ZnCo_2O_4$ exhibit higher surface area and lead to insert or extract Li^+.

According to the previous studies, several modification routines can be concluded as follows to improve electrochemical performance of $ZnCo_2O_4$ such as porous nanostructures (nanotubes,[31] nanoflakes,[32,36] nanowires,[34,37] nanorods,[38] 3D nanoparticles[39] and flower-like[40,41]), metal elements doping[42–46] and so on. The nanostructures can lead to improve the electrochemical performance of anode materials

Department of Chemical Engineering, Chung Yuan Christian University, Taiwan. E-mail: WRLiu1203@gmail.com

with higher porosity, nano size, free space and higher specific surface area because those could not only decrease the diffusion lengths but also increase the active sites for Li^+ insertion or extraction reactions. The metal elements doping method can improve the electronic conductivity and increase capacities. Another approach for ZCO modification is by carbon coating, which means coating or supporting spinel cubic $ZnCo_2O_4$ with various organic or non-organic carbon. The carbonaceous materials can provide better electronic conductivity and more stable cycle life. In addition to those, it can also buffer the volume expansion during Li^+ insertion and extraction processes.

Typically, large amount literature about $ZnCo_2O_4$ are synthesized by hydrothermal method. However, the disadvantage of conventional hydrothermal (CH) method is that it needs to take long time of reaction, wastes a lot of energy[47–54] and some Li^+ diffusion problems which will cause worse electrochemical preference such as voltage hysteresis and spinel broken spinel lattice. Contradictorily, we must to devote more energy to synthesize the alternative materials for energy storages. In addition, the heat transfers *via* conduction so compounds are heated with temperature gradient of problems. It is easier to lead materials' quality not to be uniform. Microwave irradiation that exhibits advantages, low power cost and rapid reaction time, engages our attention as a novel heating way for synthesizing nanomaterials even can produces better materials.[48] In this century, MH method has been becoming a more and more popular method for nanomaterial synthesis.

In this study, we propose a rapid microwave-assisted hydrothermal method to obtain ZCO anode materials. Microwave ZCO not only exhibit excellent electrochemical performance but also has lower impedance of resistance to charge transfer that decreases voltage hysteresis compared to conventional hydrothermal ZCO. Our previous work studied temperature effects and doping effects on $ZnCo_2O_4$.[30,55] This time, we propose an economic microwave-assisted synthesis method to prepare the novel flower-like $ZnCo_2O_4$ and compared the two samples that was synthesized through MH and CH method.

2. Experimental section

2.1. Synthesis of $ZnCo_2O_4$

The flower-like $ZnCo_2O_4$ with porous nanostructure was synthesized by using MH method. Typically, 1.5865 g of zinc nitrate hexahydrate ($Zn(NO_3)_2 \cdot 6H_2O$, 99%, SHOWA) was dissolved in ~5 mL dilute nitric acid (HNO_3, 60%, SIGMA-ALDRICH). Then add 3.1044 g cobalt nitrate hexahydrate ($Co(NO_3)_2 \cdot 6H_2O$, 98%, SHOWA) and 0.6725 g citric acid monohydrate ($C_6H_8O_7 \cdot 1H_2O$, 99.5%, SIGMA-ALDRICH) to dissolved in the above solution and added ~30 mL DI water to get the solution under continuous stirring for 10 min at pH 7 by adding ammonium hydroxide (NH_4OH, 25%, FISHER). The mixture solution was subsequently transferred to microwave oven (model no. ETHOS EASY, Milestonesrl, USA) and heated by MH method at 190 °C for 15 min. After heating, the resulting pink precipitate was air-cooled to room temperature and washed with DI water for several times. And then dried at 80 °C. The precipitate was separately annealed at 400 °C for 8 h to obtain the final products which was named M-400. For comparison conventional hydrothermal reaction was carried out, we also made the mixture solution be transferred to a 100 mL Teflon-lined stainless steel autoclave. The autoclave was heated by CH method and annealed at 400 °C named C-400 to compare MH method.

2.2. Material characterization

The products were characterized by powder X-ray diffraction (XRD, Bruker D8 Advance Eco) with Cu Kα radiation ($\lambda = 1.5418$ Å). The morphology and structure of the products were analysed by scanning electron microscopy (SEM, Hitachi S-4100) and transmission electron microscopy (TEM), then element mapping by energy-dispersive X-ray spectroscopy (EDS). The Brunauer–Emmett–Teller (BET) surface area and pore size were tested by using Micromeritics Tristar 3000. Surface analysis of the studied samples was performed using X-ray photoelectronic spectrometer (XPS).

2.3. Electrochemical measurements

The electrochemical performance of the products were measured by using CR2032 coin cells. The working electrode was composed of 70 wt% active materials, 20 wt% Super P (Carbon black, 40 nm), 6 wt% CMC and 4 wt% SBR, coating on the 10 μm copper foil, then dried at 120 °C for 8 h in vacuum system to remove the residual water. The electrolyte consisted of 1 M $LiPF_6$ in ethylene carbonate (EC) and ethyl methyl carbonate (EMC) (1 : 1 in volume ratio). The discharge/charge test were analysed by AcuTech System in the voltage range of 0.01–3.5 V at room temperature. The mass loading of these sample is ~2.4 mg cm^{-2}. The cyclic voltammograms (CV) were measured by CH Instruments Analyser CHI 6273E at a scan rate of 0.001 mV s^{-1} between 0.01 V and 3.5 V, then tested the AC impedance in the frequency range from 1–100 000 Hz in litigation state of 0.001 V.

3. Results and discussion

Fig. 1 shows the XRD patterns of $ZnCo_2O_4$ prepared with CH and MH methods. All the diffraction peaks at 2θ values of 18.89°, 31.29°, 36.84°, 38.51°, 44.82°, 55.67°, 59.35°, 65.26° and 72.28° which corresponding to the diffraction planes (111), (220), (311), (220), (400), (422), (511) and (440), respectively. As compared with the standard XRD patterns of $ZnCo_2O_4$ (JCPDS-23-1390), all these diffraction peaks could be perfectly indexed to the cubic spinel structure with XRD database in JCPDS-23-1390. Absence of any diffraction peak of Co_3O_4 and ZnO, confirmed the high purity of the products in Fig. 1. According to Scherrer's equation: $D = \kappa\lambda/\beta 1/2 \cos\theta$, where κ is shape factor, β is the line broadening at half the maximum intensity, and $\cos\theta$ is the Bragg angle, the grain size of the products was calculated with the full width at half maximum of diffraction peak (311). All the calculated average grain size of M-400 and C-400 was calculated to be about 20.4 nm and 31.3 nm, respectively. The crystal size of $ZnCo_2O_4$ *via* MH was smaller

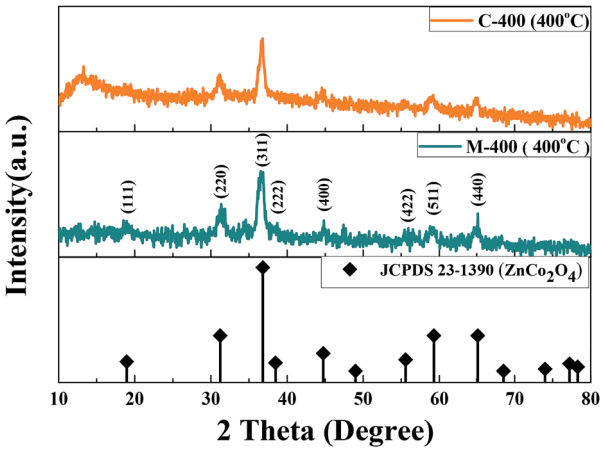

Fig. 1 XRD patterns of as-synthesized M-400 and C-400 samples.

than that of $ZnCo_2O_4$ *via* CH so it was expected the $ZnCo_2O_4$ *via* MH may demonstrate better electrochemical performances.

Fig. 2 shows the SEM images of M-400 and C-400 samples. All of them gave porous nature, especially M-400. It can be clearly seen from Fig. 2(b) that the structure consists of $ZnCo_2O_4$ uniform flower-like nanoparticles with diameters of 15–20 nm. In contrast with M-400, the structure of C-400 seemed spherical nanoparticles with larger diameters of 45–60 nm shown in Fig. 2(c) and that resulted from inconsistent heating *via* CH method. Thanks to porosity, $ZnCo_2O_4$ *via* MH method showed the great electrochemical performances. It was good for enhancing Li^+ intercalation and diffusion into the spinel lattice. Fig. 2(d) shows elements of only Zn, Co and O detected from $ZnCo_2O_4$ nanostructure, showing evidence of pure phase $ZnCo_2O_4$ in our study. Fig. 3(a)–(d) shows the EDS mapping the results, indicated that the elements Zn, Co and O were homogeneously distributed all over the structure.

TEM images of M-400 are shown in Fig. 3(e) and (f). Fig. 3(e) indicates that the size of flower-like particles are about 10–20 nm. It was similar to SEM images shown in Fig. 2(b). The

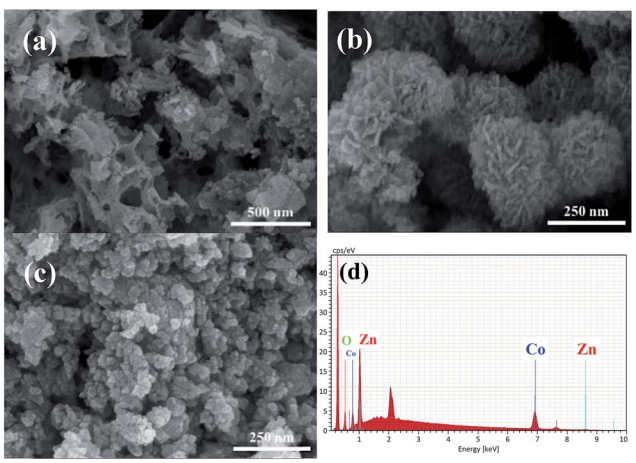

Fig. 2 SEM images of $ZnCo_2O_4$ samples: (a) M-400; high magnification of (b) M-400; (c) C-400 and (d) EDS analysis.

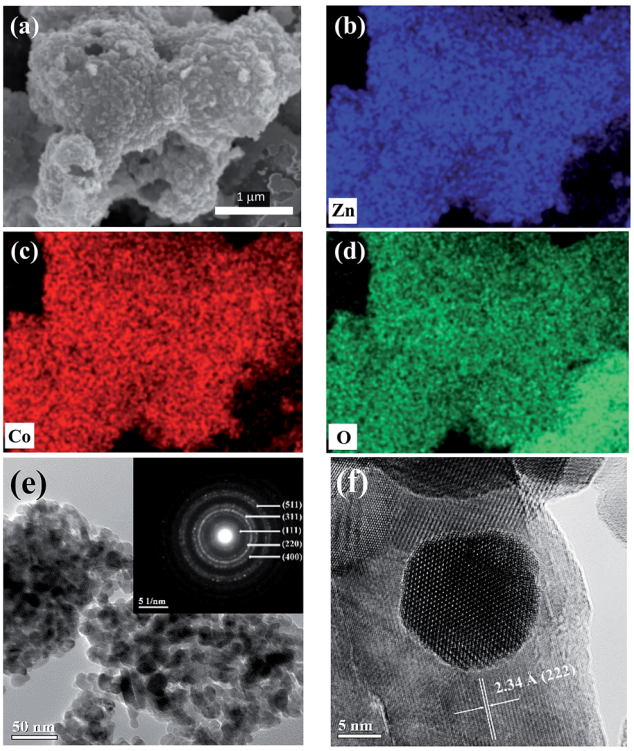

Fig. 3 (a)–(d) EDS mapping of as-prepared $ZnCo_2O_4$; (e) TEM (inset: the corresponding SAED pattern); (f) HRTEM images of M-400.

SAED pattern shown in inset of Fig. 3(e) could be well indexed by (111), (220), (311), (400) and (511) to the standard cubic spinel $ZnCo_2O_4$, respectively. As shown in Fig. 3(f), the apparent lattice spacing indicates the good crystallinity of flower-like M-400 with an interlayer distance of 2.34 Å in local domain.

The specific surface areas and pore size distribution of $ZnCo_2O_4$ nanoparticles are characterized by BET analysis using nitrogen adsorption–desorption. The unique flower-like nanostructures were expected to have larger pore sizes and high specific surface area. As shown in Fig. 4, deduced from the desorption branch based on the BJH method, $ZnCo_2O_4$ was fourth type of gas adsorption isotherms according to IUPAC classifications of hysteresis loops[37,56] and the pore size of M-400 was calculated to be about 8.97 nm. The pore sizes, shown in Fig. 4(a). In other hand, Fig. 4(b) shows there are two pore sizes of C-400 owing to inconsistent heating. It could be seen that the specific surface areas of M-400 and C-400 were about 48.8 $m^2 g^{-1}$ and 52.9 $m^2 g^{-1}$, respectively. According to previous studies,[13,35] the lattice parameters and BET surface area of other compounds displayed in Table 1. It shows that M-400 gives the smallest particle size and had shorter Li^+ diffusion distance. Such competitive BET value could be attributable to the unique structure of the flower-like nanoparticles.

The cyclic voltammograms of $ZnCo_2O_4$ samples at a scan rate of 0.1 mV s^{-1} in 0.005–3.5 V are shown in Fig. 5. According to the previous study, we believed that the Li^+ insertion and extraction reactions for the $ZnCo_2O_4$ electrode proceed as follows:[60]

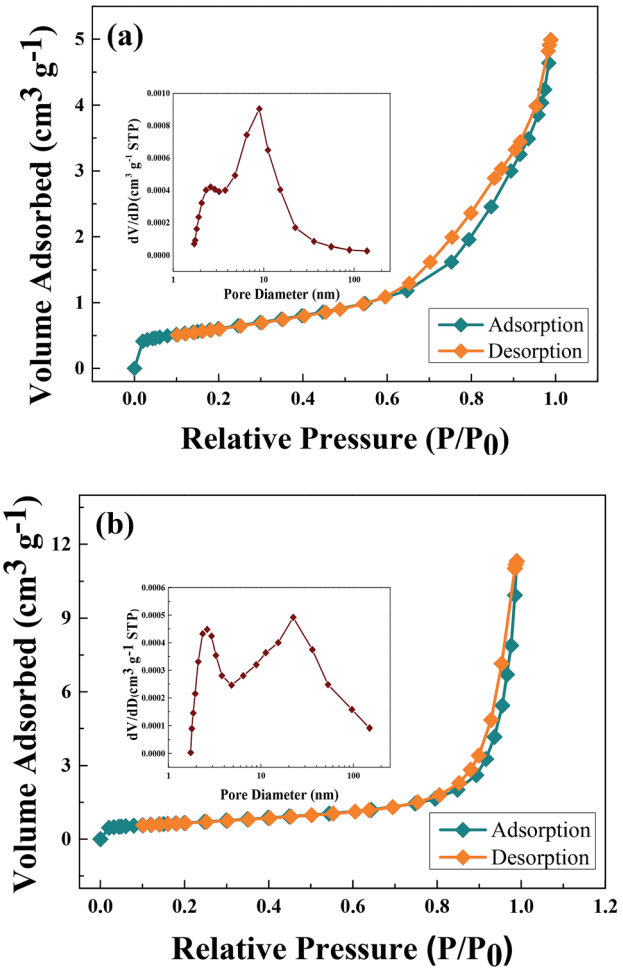

Fig. 4 N_2 adsorption–desorption isotherms and BJH pore size distributions of (a) M-400 and (b) C-400.

$$ZnCo_2O_4 + 8Li^+ + 8e^- \rightarrow Zn + 2Co + 4Li_2O \quad (1)$$

$$Zn + Li^+ + e^- \leftrightarrow LiZn \quad (2)$$

$$Zn + Li_2O \leftrightarrow ZnO + 2Li^+ + 2e^- \quad (3)$$

$$2Co + 2Li_2O \leftrightarrow 2CoO + 4Li^+ + 4e^- \quad (4)$$

$$2CoO + 2/3Li_2O \leftrightarrow 2/3Co_3O_4 + 4/3Li^+ + 4/3e^- \quad (5)$$

With the above electrochemical process, the cyclic voltammetry test (CV) and charge/discharge test can be discussed clearly below.

Fig. 5(a) shows the CVs of M-400 and C-400 in the first second cycles. It was obvious that the M-400 had a larger curve area and special current of higher redox peaks than the C-400. It was convinced that $ZnCo_2O_4$ prepared with MH method had a higher capacity and a faster kinetics for oxidation and reduction. Moreover, this was learned from the results of charge/discharge tests. The reduction peak in the first cycle shows an intense irreversible reaction at ~0.55 V in the first cathodic process because of the decomposition of $ZnCo_2O_4$ to Zn^0 and Co^0 according to eqn (1) with the formation of a solid electrolyte interphase (SEI). In the voltage range of 0.005–1.0 V, the absence of well-defined peaks in the CV and voltage plateaus in the voltage–capacity profiles corresponding to the oxidation/reduction of Zn according to eqn (2).[19,61] In previous study,[35] we can see that similar potential also appeared the reduction peak because of the same reason. According to report from Reddy *et al.*,[27] optimum specific surface area, morphology and defect-free crystal structure of $ZnCo_2O_4$ would impact on formation of SEI. Compared with the discharge of the second cycle which could be ascribed to the alleviation of electrode polarization, the peaks found at ~0.7 V, indicative of different electrochemical reactions occurs at two process. However, oxidation peaks at ~1.7 V and 2.2 V in the anodic polarization, which could be attributed to the oxidation of Zn^0 to Zn^{2+} and Co^0 to Co^{3+} (eqn (3)–(5)) respectively. Addition to oxidation peaks at ~0.25 V, the reaction is resulted from graphitic material or LiZn alloy.[62] From the previous data, we knew our mechanisms for M-400 and C-400 are the same as previous study.

Fig. 6(a) shows charge/discharge curves of M-400 at current density of 0.1C in the voltage range of 0.01–3.5 V in the first three cycles. It could clearly be observed that a plateau at ~0.5 V was in the first charging process. For the second and third cycles, the plateau shifts to ~1.25 V and became steeper, which was in consist with the CV results shown in Fig. 5(a). The initial charge and discharge capacity were 1511 and 1220 mA h g^{-1}, respectively. The coulombic efficiency in the first cycle was as high as 80.8%. The irreversible capacity loss in the first cycle was ~16.3%, which was associated with the formation of SEI film. Because of the reduction of solvents in the electrolyte,

Table 1 Morphology, lattice constants, particle size, surface area, the charge/discharge capacities at the 1st C/D cycle and discharge capacity at the 50th

Compounds	Morphology	Lattice constants (Å)	Particle size (nm)	Surface area (m^2 g^{-1})	1st C/D capacities (mA h g^{-1})	50th discharge capacity (mA h g^{-1})
M-400 (this study)	Flower-like	8.1	10–20	48.8	1511/1220	1373 (0.2 A g^{-1})
ZCO[35]	Spherical	8.1	10–20	11.5	1400/960	N/A
ZCO[57]	Hollow	N/A	250–300	25.0	NA/1442	600 (3 A g^{-1})
ZCO@C[57]	Yolk–shell	N/A	50–80	20.0	NA/1409	700 (3 A g^{-1})
ZCO@PPy/SA[58]	Lychee-like	N/A	250	36.2	NA/NA	590 (0.1 A g^{-1})
ZCO/ZnO[59]	Nanoplate-like	N/A	630–800	60.3	1599/1071	N/A
ZCO/ZnO/C[42]	Core/shell	8.1	800	27.9	1279/974	800 (0.5 A g^{-1})

crystal structure would destruct to format SEI film and Li^+ was consumed to cause capacity loss.[63,64] In addition, it maybe the nanostructure was changed in Li^+ diffusion process.[27,64] This might be a result of the volume variations and crystal structure modifications during cycling.[64] The second discharge cycle and third discharge cycle were 1264 and 1277 mA h g^{-1} and the charge/discharge curves all most overlap, indicating the great reversibility electrochemical properties of M-400 and the result well matched with the CV results. As shown Fig. 6(b), the initial discharge capacity of C-400 is 1438 mA h g^{-1}, respectively. Irreversible capacity loss in the first cycle was ~22.2%, respectively. It took advantage of MH method to turn into the smaller crystal size and good for the electrochemical performances.

Fig. 7(a) shows the cycling performance of M-400 and C-400 at current density of 0.2C. Clearly, it could be observed the initial discharge capacity of C-400 was the highest one, 1410 mA h g^{-1}, of all samples but it was declining after 10 cycles. Compared to C-400, the discharge of capacity indicated that the capacity of M-400 not only did not decline but also increased, exhibited the better cycling performance. After 45 cycles, the reversible capacities of M-400 and C-400 are 1411, and 217 mA h g^{-1}, respectively. According to the previous study,[39,65] the reversible capacity slightly, in addition, increased with cycling and remained above 1000 mA h g^{-1} at after 45 cycles at current density of 0.2C. At all samples, it might be attributed to the largest porosity of nanoparticle structure to cause capacity of M-400 to remain the higher capacity and good retention. The XRD and the BET resulted shown in Fig. 1 and 4, the smaller crystal size and higher surface area of M-400 provided Li-ion the shorter diffusion distance and enhanced to contact areas between the electrolyte and $ZnCo_2O_4$, exhibited better capacity retained ability than other samples.

As shown in Fig. 7(b), the cycling performance of M-400 and C-400 at different current densities from 0.1C to 10C. The average discharge capacity of C-400 decreases from 1345, 461, 44 to 13 mA h g^{-1} with increasing the current densities from 0.1C, 1C, 5C, and 10C, whereas the average discharge capacity of M-400 was 605 mA h g^{-1} at the current density of 10C. In the subsequent cycles, the capacity recovered to 1665 mA h g^{-1} with the current density back to 0.1C, even higher than original capacity. Clearly, the samples *via* MH method delivered higher discharge capacity than one *via* CH method at all tested current densities. Thanks to flower-like nano-structure, Li-ion could be easier to pass through in diffusion process and it made sure that the cycling stability and rate capability were better than one in CH method. Fig. 7(c) demonstrated that the coulombic efficiency of M-400 in the 180 cycles closed to 100% efficiency indicating its great cyclic ability. Obviously, the reversible capacity of M-400 could be maintaining to ~630 mA h g^{-1} after 180 cycles which was ~1.7 times than that of graphite anode.

The result of AC impedance is investigated to understand the kinetics that influences the performances toward lithium after charging at the third cycle shown in Fig. 7. The diameters of the semicircles for M-400 and C-400 are 144 Ω and 485 Ω, respectively. M-400 exhibited the lowest impedance that went toward diffusion process. In order to learn the major contribution of impedance in these the samples. It could be analyzed with a typical equivalent circuit shown in the inset in Fig. 7(e).

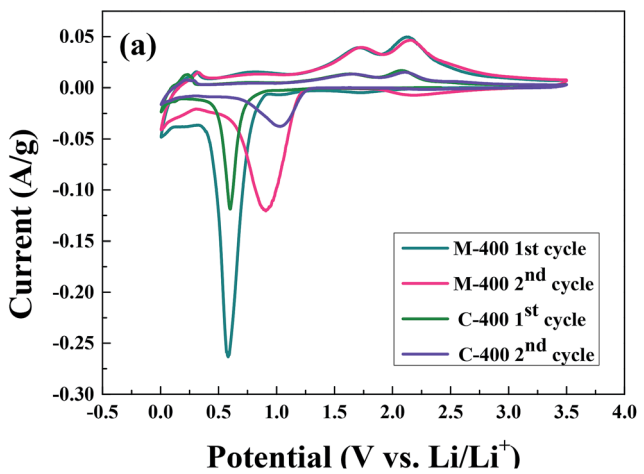

Fig. 5 (a) The first second cycles of CVs for M-400 and C-400 at a scan rate of 0.1 mV s^{-1}.

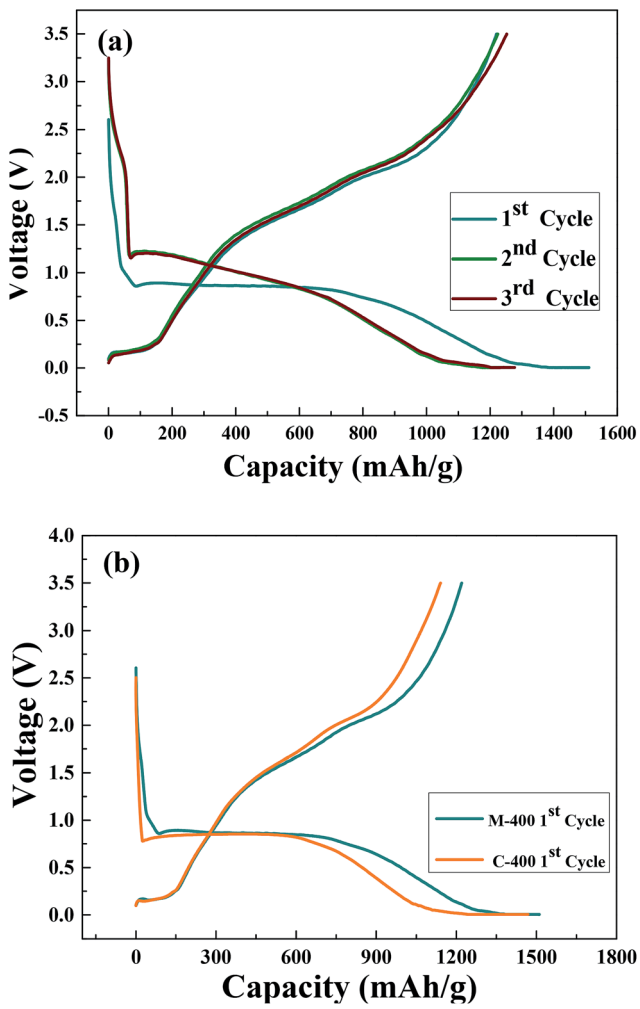

Fig. 6 (a) First three cycles discharge/charge curves of M-400; (b) first cycle discharge/charge curves of M-400 and C-400.

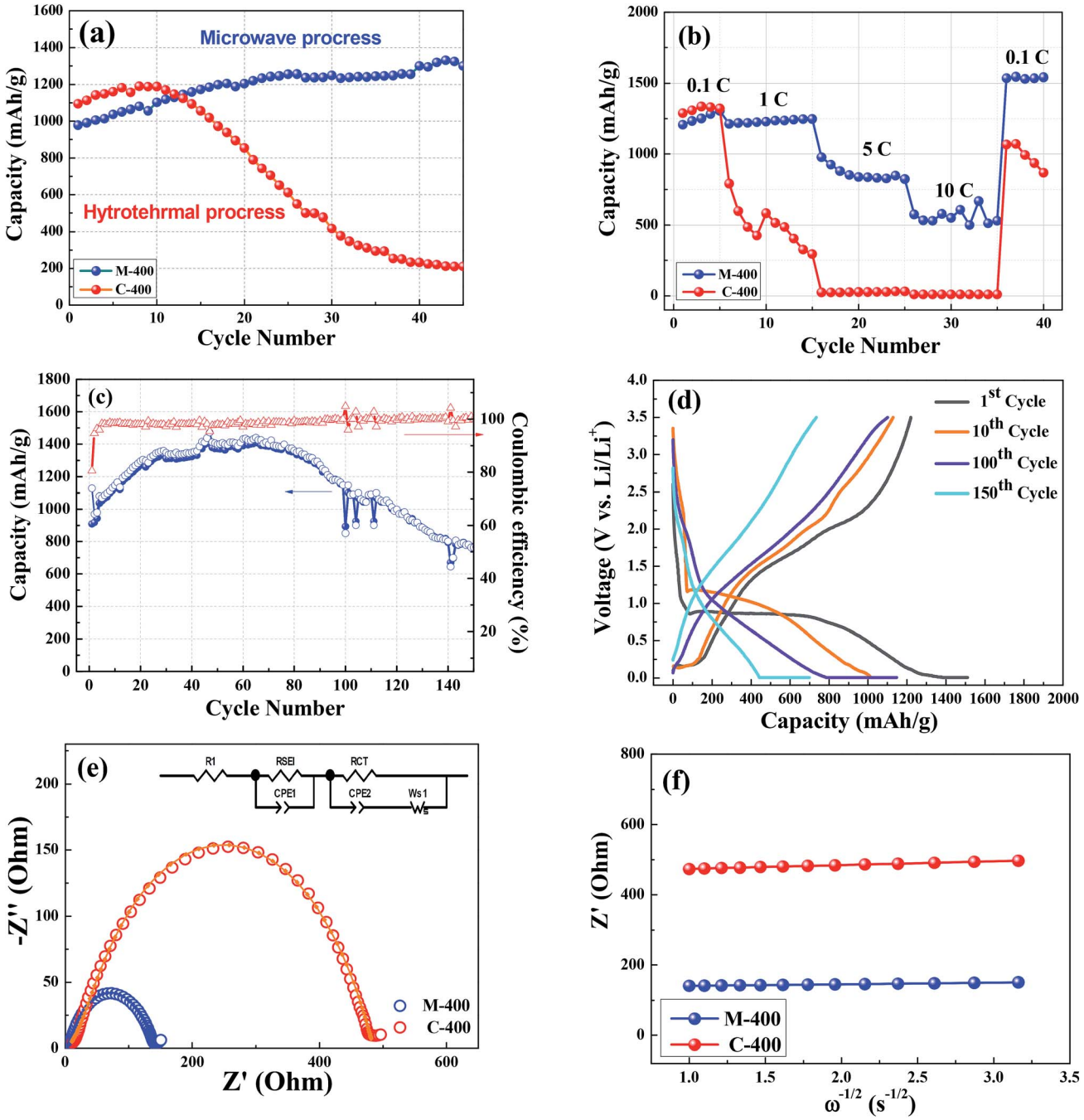

Fig. 7 (a) Cycling performance of M-400 and C-400 for 45 cycles at 0.2C; (b) C-rate performance of M-400 and C-400; (c) cycling performance and columbic efficiency of M-400 for 150 cycles at 0.2C; (d) 180 cycles discharge/charge curves of M-400; (e) AC impedance (inserting the fitted equivalent circuit) of M-400 and C-400 at the third cycle; (f) plot Z' *vs.* $\omega^{-1/2}$ at low frequency.

Herein, R_1, R_{SEI}, R_{CT} and W_s were impedances resulted from electrolyte, SEI film, charge transfer and Warburg impedance[61] of $ZnCo_2O_4$, respectively. Some of the corresponding fitting data were displayed in Table 2. Comparing to samples, R_1 and R_{SEI} values were almost close since impedance of interface between electrode and electrolyte were similar. Obviously, the dramatic difference in impedance was charge transfer resistance. The R_{CT} of M-400 and C-400 are 79.5 Ω and 419.2 Ω, respectively. According to fitting data, the R_{CT} was increasing by higher annealing temperature and $ZnCo_2O_4$ *via* MH method exhibited smaller impedance than one *via* CH method. This indicated that microwave heating was favorable to improve the conductivity of $ZnCo_2O_4$, and then led to the improvement of electrochemical properties. Besides, the porous characteristic was good for the reaction kinetics and diffusion of Li ion. Further details on equivalent electrical circuit notations are discussed by Reddy *et al.*[61,64,66] W_s is associated with the solid state diffusion of Li-ion through the

Table 2 Impedance parameters calculated from equivalent circuit model

$ZnCo_2O_4$	R_1 (Ω)	R_{SEI} (Ω)	R_{CT} (Ω)	σ_w	D ($cm^2\ s^{-1}$)
M-400	4.8	60.0	79.5	4.5	4.6×10^{-11}
C-400	3.8	62.8	419.1	19.3	2.5×10^{-12}

$ZnCo_2O_4$ lattice. The Li^+ diffusion coefficient can be calculated by the following equation.[67]

$$D = \frac{R^2T^2}{2A^2n^4F^4C^2\sigma_w{}^2} \quad (6)$$

where R is the gas constant (8.314 J K^{-1} mol^{-1}), T is the absolute temperature (293.15 K) at room temperature, A is the surface area of the electrode (~1.54 cm^2), n is the number of electrons per molecule during oxidization ($n = 2$), F is Faraday's constant (96 500 C mol^{-1}), and C is the concentration of lithium ions (0.001 mol cm^{-3}). According to the eqn (6), diffusion coefficients of lithium among M-400 and C-400 were calculated to be 4.6×10^{-11} cm^2 s^{-1} and 2.5×10^{-12} cm^2 s^{-1}, respectively. Obviously, diffusivity of Li^+ in M-400 was much higher than that of C-400.

4. Conclusions

A rapid and economic microwave-assisted synthesis method has improved to prepare novel nano-porous flower-like $ZnCo_2O_4$ anode materials for lithium-ion batteries. In summary, $ZnCo_2O_4$ anode with high-quality samples is successfully synthesized by MH method. The XRD analysis identifies a cubic lattice structure. The SEM and TEM images show that M-400 with diameters about 15–20 nm could be obtained. The BET results show that the specific surface areas is decreasing when annealing temperature increasing. $ZnCo_2O_4$ *via* MH method that pore size is single is good for electrochemical performance. The flower-like $ZnCo_2O_4$ shows high capacity, great rate capability and cyclic stability performance. The initial charge capacity of M-400 can reach as high as 1510 mA h g^{-1} at current density of 0.1C, because of the short diffusion distance. After 150 cycles, the capacity still maintains 630 mA h g^{-1} at current density of 0.2C. The AC impedance results future proves that M-400 gives the lowest surface layer resistance. All the results indicate that $ZnCo_2O_4$ is a promising and novel anode candidate for high-performance LIBs. Furthermore, MH method is more efficient and eco-friendly route to obtain spinel oxides with a flower-like structure.

Conflicts of interest

There are no conflicts to declare.

Acknowledgements

The authors would like to thanks the financial support by National Science Council under contract no. of NSC-105-2815-C-033-047-E.

Notes and references

1 H. Li, Z. Wang, L. Chen and X. Huang, *Adv. Mater.*, 2009, **21**, 4593–4607.
2 B. Scrosati and J. Garche, *J. Power Sources*, 2010, **195**, 2419–2430.
3 A. Cooper, *J. Power Sources*, 2004, **133**, 116–125.
4 E. Karden, S. Ploumen, B. Fricke, T. Miller and K. Snyder, *J. Power Sources*, 2007, **168**, 2–11.
5 M. Perrin, Y. Saint-Drenan, F. Mattera and P. Malbranche, *J. Power Sources*, 2005, **144**, 402–410.
6 Y. Wu, P. Zhu, M. Reddy, B. Chowdari and S. Ramakrishna, *ACS Appl. Mater. Interfaces*, 2014, **6**, 1951–1958.
7 M. Armand and J.-M. Tarascon, *Nature*, 2008, **451**, 652–657.
8 P. G. Bruce, B. Scrosati and J. M. Tarascon, *Angew. Chem., Int. Ed.*, 2008, **47**, 2930–2946.
9 P. Simon and Y. Gogotsi, *Nat. Mater.*, 2008, **7**, 845–854.
10 D. Darbar, M. Reddy, S. Sundarrajan, R. Pattabiraman, S. Ramakrishna and B. Chowdari, *Mater. Res. Bull.*, 2016, **73**, 369–376.
11 M. Reddy, T. Yu, C.-H. Sow, Z. X. Shen, C. T. Lim, G. Subba Rao and B. Chowdari, *Adv. Funct. Mater.*, 2007, **17**, 2792–2799.
12 X. Zhu, Y. Zhu, S. Murali, M. D. Stoller and R. S. Ruoff, *ACS Nano*, 2011, **5**, 3333–3338.
13 M. Reddy, C. Y. Quan, K. W. Teo, L. J. Ho and B. Chowdari, *J. Phys. Chem. C*, 2015, **119**, 4709–4718.
14 M. Reddy, C. T. Cherian, K. Ramanathan, K. C. W. Jie, T. Y. W. Daryl, T. Y. Hao, S. Adams, K. Loh and B. Chowdari, *Electrochim. Acta*, 2014, **118**, 75–80.
15 C. T. Cherian, J. Sundaramurthy, M. V. Reddy, P. Suresh Kumar, K. Mani, D. Pliszka, C. H. Sow, S. Ramakrishna and B. V. R. Chowdari, *ACS Appl. Mater. Interfaces*, 2013, **5**, 9957–9963.
16 B. Varghese, M. Reddy, Z. Yanwu, C. S. Lit, T. C. Hoong, G. Subba Rao, B. Chowdari, A. T. S. Wee, C. T. Lim and C.-H. Sow, *Chem. Mater.*, 2008, **20**, 3360–3367.
17 Y. Li, B. Tan and Y. Wu, *Nano Lett.*, 2008, **8**, 265–270.
18 Z. Wang and L. Zhou, *Adv. Mater.*, 2012, **24**, 1903–1911.
19 M. Reddy, L. Y. T. Andreea, A. Y. Ling, J. N. C. Hwee, C. A. Lin, S. Admas, K. Loh, M. K. Mathe, K. I. Ozoemena and B. Chowdari, *Electrochim. Acta*, 2013, **106**, 143–148.
20 Y. Sharma, N. Sharma, G. Subba Rao and B. Chowdari, *Adv. Funct. Mater.*, 2007, **17**, 2855–2861.
21 M. Reddy, Z. Beichen, L. J. E. Nicholette, Z. Kaimeng and B. Chowdari, *Electrochem. Solid-State Lett.*, 2011, **14**, A79–A82.
22 M. Reddy, C. Yu, F. Jiahuan, K. P. Loh and B. Chowdari, *RSC Adv.*, 2012, **2**, 9619–9625.
23 M. Chhowalla, H. S. Shin, G. Eda, L.-J. Li, K. P. Loh and H. Zhang, *Nat. Chem.*, 2013, **5**, 263–275.
24 J. B. Goodenough and Y. Kim, *Chem. Mater.*, 2009, **22**, 587–603.
25 C.-M. Park, J.-H. Kim, H. Kim and H.-J. Sohn, *Chem. Soc. Rev.*, 2010, **39**, 3115–3141.

26 B. Das, M. Reddy and B. Chowdari, *J. Alloys Compd.*, 2013, **565**, 90–96.
27 M. V. Reddy, C. Yu, F. Jiahuan, K. P. Loh and B. V. R. Chowdari, *ACS Appl. Mater. Interfaces*, 2013, **5**, 4361–4366.
28 A. S. Hameed, H. Bahiraei, M. Reddy, M. Z. Shoushtari, J. J. Vittal, C. K. Ong and B. Chowdari, *ACS Appl. Mater. Interfaces*, 2014, **6**, 10744–10753.
29 M. Reddy, Y. Xu, V. Rajarajan, T. Ouyang and B. Chowdari, *ACS Sustainable Chem. Eng.*, 2015, **3**, 3035–3042.
30 J.-X. Fu, W.-T. Wong and W.-R. Liu, *RSC Adv.*, 2015, **5**, 75838–75845.
31 W. Luo, X. Hu, Y. Sun and Y. Huang, *J. Mater. Chem.*, 2012, **22**, 8916–8921.
32 Y. Qiu, S. Yang, H. Deng, L. Jin and W. Li, *J. Mater. Chem.*, 2010, **20**, 4439–4444.
33 Y. Zhu, C. Cao, J. Zhang and X. Xu, *J. Mater. Chem. A*, 2015, **3**, 9556–9564.
34 N. Du, Y. Xu, H. Zhang, J. Yu, C. Zhai and D. Yang, *Inorg. Chem.*, 2011, **50**, 3320–3324.
35 M. Reddy, K. Kenrick, T. Y. Wei, G. Y. Chong, G. H. Leong and B. Chowdari, *J. Electrochem. Soc.*, 2011, **158**, A1423–A1430.
36 T.-F. Hung, S. G. Mohamed, C.-C. Shen, Y.-Q. Tsai, W.-S. Chang and R.-S. Liu, *Nanoscale*, 2013, **5**, 12115–12119.
37 H. Chen, Q. Zhang, J. Wang, Q. Wang, X. Zhou, X. Li, Y. Yang and K. Zhang, *Nano Energy*, 2014, **10**, 245–258.
38 H. Liu and J. Wang, *Electrochim. Acta*, 2013, **92**, 371–375.
39 S. Grugeon, S. Laruelle, L. Dupont and J.-M. Tarascon, *Solid State Sci.*, 2003, **5**, 895–904.
40 W. Fu, X. Li, C. Zhao, Y. Liu, P. Zhang, J. Zhou, X. Pan and E. Xie, *Mater. Lett.*, 2015, **149**, 1–4.
41 S. G. Mohamed, T.-F. Hung, C.-J. Chen, C. K. Chen, S.-F. Hu, R.-S. Liu, K.-C. Wang, X.-K. Xing, H.-M. Liu and A.-S. Liu, *RSC Adv.*, 2013, **3**, 20143–20149.
42 X. Ge, Z. Li, C. Wang and L. Yin, *ACS Appl. Mater. Interfaces*, 2015, **7**, 26633–26642.
43 P. F. Teh, S. S. Pramana, Y. Sharma, Y. W. Ko and S. Madhavi, *ACS Appl. Mater. Interfaces*, 2013, **5**, 5461–5467.
44 L. Wu, Q. Xiao, Z. Li, G. Lei, P. Zhang and L. Wang, *Solid State Ionics*, 2012, **215**, 24–28.
45 X. Song, Q. Ru, Y. Mo, L. Guo, S. Hu and B. An, *J. Power Sources*, 2014, **269**, 795–803.
46 J.-P. Zhou, L. Li and X.-Z. Chen, *J. Ceram. Process Res.*, 2010, **11**, 263–272.
47 J.-H. Lee, C.-K. Kim, S. Katoh and R. Murakami, *J. Alloys Compd.*, 2001, **325**, 276–280.
48 Y. Wang, J. Ke, Y. Zhang and Y. Huang, *J. Mater. Chem. A*, 2015, **3**, 24303–24308.
49 L. Wang, X. Zhang, Y. Ma, M. Yang and Y. Qi, *Mater. Lett.*, 2016, **164**, 623–626.
50 X. Lu, Z. Wang, L. Lu, G. Yang, C. Niu and H. Wang, *Inorg. Chem.*, 2016, **55**, 7012–7019.
51 Y. J. Yun, J. K. Kim, J. Y. Ju, S. Unithrattil, S. S. Lee, Y. Kang, H.-K. Jung, J.-S. Park, W. B. Im and S. Choi, *Dalton Trans.*, 2016, **45**, 5064–5070.
52 D. Yuan, G. Huang, F. Zhang, D. Yin and L. Wang, *Electrochim. Acta*, 2016, **203**, 238–245.
53 A. Shanmugavani and R. K. Selvan, *Electrochim. Acta*, 2016, **188**, 852–862.
54 X. Zhou, J. Shi, Y. Liu, Q. Su, J. Zhang and G. Du, *J. Alloys Compd.*, 2014, **615**, 390–394.
55 W. T. Wong, B. H. Chen, I. V. B. Maggay, C. Liu, J. G. Duh and W. R. Liu, *Energy Technol.*, 2017, DOI: 10.1002/ente.201600634.
56 T. Liu, J. Liu, Q. Liu, D. Song, H. Zhang, H. Zhang and J. Wang, *Nanoscale*, 2015, **7**, 19714–19721.
57 S. H. Choi and Y. C. Kang, *ChemSusChem*, 2013, **6**, 2111–2116.
58 L. Zhang, J. Zheng, P. Dou, W. Wang, J. Cheng and X. Xu, *J. Mater. Sci.: Mater. Electron.*, 2017, 1–9.
59 C. W. Lee, S.-D. Seo, D. W. Kim, S. Park, K. Jin, D.-W. Kim and K. S. Hong, *Nano Res.*, 2013, **6**, 348–355.
60 M. Reddy, G. Subba Rao and B. Chowdari, *Chem. Rev.*, 2013, **113**, 5364–5457.
61 M. Reddy, G. S. Rao and B. Chowdari, *J. Mater. Chem.*, 2011, **21**, 10003–10011.
62 S. Petnikota, N. K. Rotte, V. V. Srikanth, B. S. Kota, M. Reddy, K. P. Loh and B. Chowdari, *J. Solid State Electrochem.*, 2014, **18**, 941–949.
63 C. T. Cherian, M. Zheng, M. Reddy, B. Chowdari and C. H. Sow, *ACS Appl. Mater. Interfaces*, 2013, **5**, 6054–6060.
64 M. V. Reddy, B. L. Wei Wen, K. P. Loh and B. V. R. Chowdari, *ACS Appl. Mater. Interfaces*, 2013, **5**, 7777–7785.
65 S.-H. Yu, S. H. Lee, D. J. Lee, Y.-E. Sung and T. Hyeon, *Small*, 2016, **12**, 2146.
66 M. Reddy, S. Madhavi, G. S. Rao and B. Chowdari, *J. Power Sources*, 2006, **162**, 1312–1321.
67 W. Duan, Z. Zhu, H. Li, Z. Hu, K. Zhang, F. Cheng and J. Chen, *J. Mater. Chem. A*, 2014, **2**, 8668–8675.